Metals and Materials International (2021) 27:1147–1154
https://doi.org/10.1007/s12540-020-00618-8

Effect of Mechanical Alloying on the Microstructural Evolution of $Al_{60}Cr_{30}Si_{10}$ Alloys Processed by Spark Plasma Sintering

Jeong-Han Lee[1,2] · Ik-Hyun Oh[1] · Jun-Ho Jang[1] · Ju-Hun Kim[1,2] · Sung-Kil Hong[2] · Hyun-Kuk Park[1]

Received: 19 November 2019 / Accepted: 9 January 2020 / Published online: 1 February 2020

Abstract
In this study, Al, Cr and Si fine powders were alloyed by planetary ball milling to investigate their microstructural evolution, following their mechanical alloying behavior. The formation of Al(Cr) supersaturated solid solution by the Cr grains embedded in Al-matrix, which contributed substitutional structure is discussed in relation to their structural evolution in accordance with the distortion of a crystal lattice. The compacts of Al–Cr–Si alloys were prepared by rapid sintering within a short time by dense consolidation above the density of 99.9% as the formation of intermetallics, except in the case of the distribution of single-phases induced by the Al-melting. The formation behavior of intermetallics was dominated by dependence on the structures of the milled-powder and subsequent sintering temperature. To estimate the consolidated behaviors of compacts, various approaches derived from TEM and XRD analysis were taken to obtain microstructural evidences of the inter-diffusion, following the presence of thermally stable intermetallics.

Keywords Al–Cr–Si · Powder characteristics · Mechanical alloying · Spark plasma sintering · Intermetallics

1 Introduction

Al–Cr–Si ternary alloys are typical coating materials that can replace the PVD hard-coated films, such as Ti-based and Cr-based materials (e.g. TiN, TiAlN, CrN, CrWN, and $CrN + MoS_2N$, etc.), and show good oxidation resistance that is suitable for application at high-temperature [1–3]. In particular, the mechanical and thermal properties can be predominantly determined depending on the additional composition of films of ternary elements, with their results being reported in several studies [4, 5].

Crystallographically, the structure of Al_xCr_{1-x} can be variably transformed depending on the contents of 'x' (atomic percent), and its properties can be determined [6, 7]. For example, in the range ($0.6 < x < 0.7$), Al–Cr consists of NaCl structure (FCC), and is thermodynamically very stable. However, in the range ($x > 0.7$), Al–Cr is transformed to a Wurtzite structure (HCP), forming thin films in which the Al-component takes precedence, to provide thermal stability and good oxidation resistance (> 900 °C), but the mechanical properties are deteriorated [6, 7]. To enhance the mechanical properties by the addition of Si of (5–20) at%, it is possible to improve the mechanical and thermal properties of thin films by forming amorphous Si_3N_4 by suppressing the grain growth of nanocrystalline, and by expressing strong cohesive energy [8, 9].

However, few studies have yet reported the microstructural behavior of intermetallics following the fabrication of multi-component Al–Cr–Si alloys used as coating targets materials, except for their thermodynamic description or modeling [10–12]. Notably, in order to overcome the challenges of limited mechanical and thermal properties in the AlCr-based alloys, they could be improved by several means: (1) Imparting of solid solution strengthening and even grain refining, e.g. severe plastic deformation and mechanical alloying [13], (2) Fabricated rapidly densifying sintered-compacts for multi-component elements having a different melting point, e.g. spark plasma sintering, (3) Formation of intermetallics with inter-diffusion by means of additive elements, e.g. Cr: preventing recrystallization [10], Si: stability

✉ Hyun-Kuk Park
hk-park@kitech.re.kr

[1] EV&Components Materials Group, Korea Institute of Industrial Technology (KITECH), 6, Cheomdan-gwagiro 208-gil, Buk-gu, Gwangju 61012, Republic of Korea

[2] Materials Science and Engineering, Chonnam National University, 77, Yong-bongro, Buk-gu, Gwangju 61186, Republic of Korea

at the high temperature [14], and (4) Microstructural evidence of two-sublattices with intermetallics [15, 16].

Consequently, this study is to clarify experimental evidence for the formation of intermetallics related to structural evolution, in which the $Al_{60}Cr_{30}Si_{10}$ alloys are prepared by mechanical alloying using planetary ball milling, followed by powder metallurgy using a spark plasma sintering method.

2 Experimental Procedure

Initial powders of Al (Ave. 9.2 μm), Cr (Ave. 17.5 μm), and Si (Ave. 20.1 μm) with purity of 99.9% were used for mechanical alloying (MA). These powders were alloyed mechanically aimed at the composition of $Al_{60}Cr_{30}Si_{10}$. Table 1 shows details of the MA parameters.

To produce dense compacts, the $Al_{60}Cr_{30}Si_{10}$ alloys were consolidated to form intermetallics by means of spark plasma sintering in the temperature range (560–1100) °C with 60 °C/min heating rate and under 60 MPa sintering pressure in a short time (within 18 min). The relative densities of compacts were then measured by the Archimedes method, i.e. compared to the theoretical density (approximately 3.69 g/cm^3) of $Al_{60}Cr_{30}Si_{10}$ compacts.

The grain size and internal strain of Al(Cr) supersaturated solid solutions in alloyed powder were measured by Stokes and Wilson's formula [17] using the XRD patterns:

$$b = b_d + b_e = k\lambda/(d\cos\theta) + 4\varepsilon\tan\theta \quad (1)$$

In Eq. (1), b is the full-width at half-maximum (FWHM) of the mechanical correction value of the diffraction peak, and b_d and b_e are the measured values of the decrease by internal stress and the FWHM. k is the Scherr constant of 0.9, λ is the X-ray radiation wavelength using CuKα radiation (1.5406 Å), d and ε are the measurements of the grain size and internal strain, respectively, and θ is the Bragg's angle.

To clarify the structural evolution from $Al_{60}Cr_{30}Si_{10}$ milled powder, their compacts were investigated depending on the milling times using the XRD patterns with peak shifting and broadening, in which the corresponding single phase or intermetallics were referred to phase indexing to match the Joint committee on powder diffraction standards (JCPDS) card provided by High-Score Plus application.

Furthermore, in order to demonstrate the microstructural evolution, the $Al_{60}Cr_{30}Si_{10}$ compacts were investigated depending on sintering temperature using the TEM analysis, and subjected to enlarged HR images or FFT diffraction patterns that were identified clearly with the distribution of intermetallics that indicated the presence of the two sublattices. In particular, the estimated phases for the intermetallics within microstructure were examined by means of the SEM–EDS.

Table 1 Mechanical alloying parameters by planetary ball milling for $Al_{60}Cr_{30}Si_{10}$ synthesized powders

Composition	Milling time (h)	Rotation speed (rpm)	Atmosphere	Ball:powder (wt%)	PCA
$Al_{60}Cr_{30}Si_{10}$	5, 15, 25	250	Ar gas	15:1	Ethanol (4 wt%)

3 Results and Discussion

Figure 1 shows the microstructure of the $Al_{60}Cr_{30}Si_{10}$ alloy powder according to milling time. As the milling time increased, following MA in a randomly distributed state of the initial single-phase, a supersaturated solid solution is formed by a severe plastic deformation [18, 19] (SPD). In other words, their MA behaviors were divided into two major mechanisms, i.e. ductile–ductile and ductile–brittle components [20–22]. The Al–Cr system with ductile–ductile components underwent the initial stage to be flattened by micro-forging [23]. The micro-morphologies that occurred were from flattened agglomerates (see Fig. 1b Al_xCr_y) to form cold welded mutually forming lamellar structure corresponding to work hardening [23]. As the interlamellar spacing decreased accompanying the lattice defect concentration, particles tended to reach saturation stage with the formation of solid solution (see Fig. 1c Al(Cr)).

On the other hand, in the Cr–Si system with ductile–brittle component, brittle particles tend to be trapped into ductile particles. With further milling, chemically homogeneous intermetallics are formed with the solubility of Si into Cr. However, the SPD that may impair the solid solubility collapsed this chemical bonding in Cr_xSi_y structures, which induced precipitation into a single-phase of Si (see Fig. 1c Si). Consequently, the Cr particle was rapidly refined simultaneously with the decrease of interlamellar spacing to accelerate the formation of solid solution [21, 22] (see Fig. 1c Al(Cr)) with the Al-matrix.

Figure 2 shows the formation behavior of the Al(Cr) supersaturated solid-solution according to the milling time in relation to their structural evolution. The lattice parameter of Al decreases (4.032 → 4.014) Å, see JCPDS 04-4713 [24]) with the formation of intermetallics by the MA behavior at the 15 h-milled; even so, the volume of unit cell also shrinks (65.54 → 64.67) × 10^6 pm^3, see JCPDS 04-4713 [24]). In addition, the Al_xCr_y intermetallics were substituted by Cr in the Al-matrix due to the difference in ion radius between Al (1.431 Å) and Cr (1.249 Å), causing compressive stress. As reported in the Hume-Rothery theory [25],

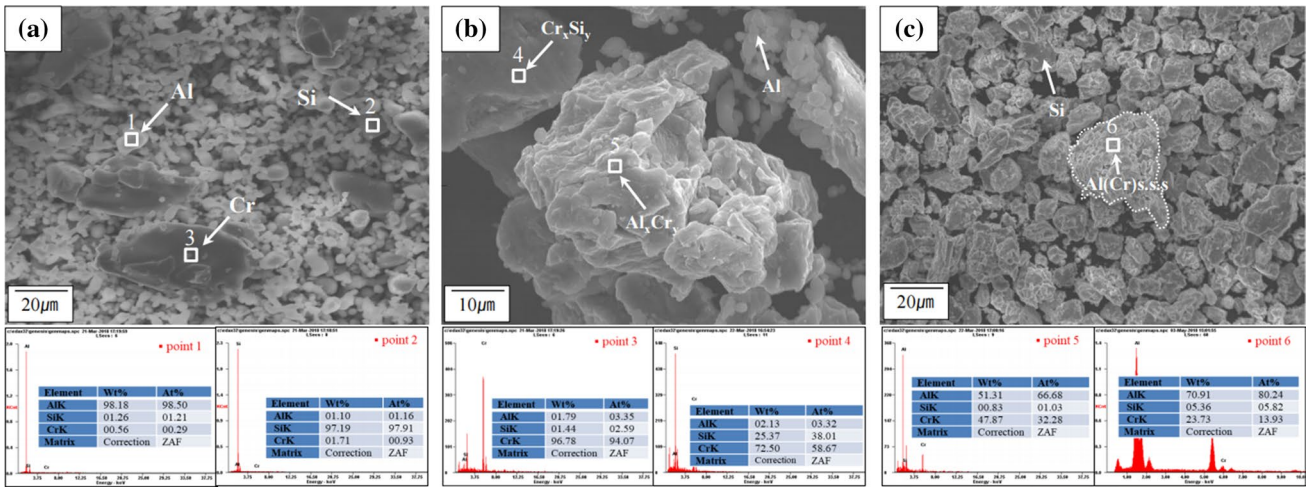

Fig. 1 Microstructural morphology their EDS results of $Al_{60}Cr_{30}Si_{10}$ powders with different milling time: **a** 5 h, **b** 15 h, and **c** 25 h

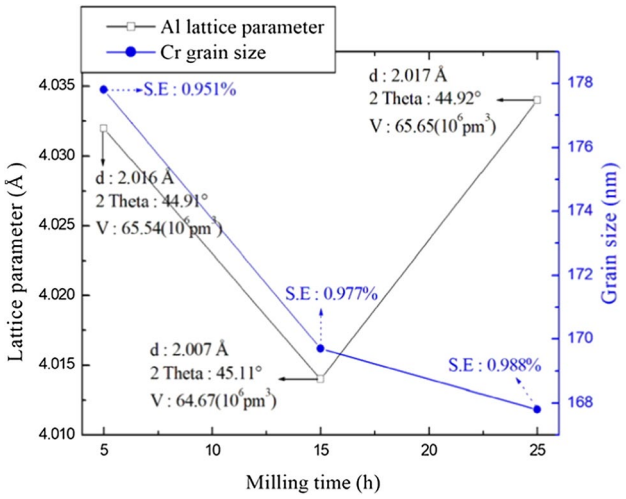

Fig. 2 Structural evolution of Al and Cr grains with their lattice parameters for different milling times

when the difference in size between the solute and solvent atoms is less than 15%, there is a strong tendency to form a solid solution. In other words, it can be determined that the formation of a substitutional solid solution is promoted, because the atomic radius ratio of the Al/Cr atoms represents a difference of about 13% in this work. Furthermore, in Al(Cr) supersaturated solid solution at 25 h-milled, the tendency of Cr to precipitate by the grain refinement accumulates [26] irregular strain and potential energy inside the lattice of the particle. Due to these two internal energies, tensile stress is applied, considering that the lattice parameter increases (4.014 → 4.034) Å, see JCPDS 89-2871 [27]).

The XRD patterns shown in Fig. 3 confirm that the structural evolutions are related to the microstructures of the $Al_{60}Cr_{30}Si_{10}$ alloy powder mentioned in Fig. 1. In particular, Fig. 3b shows the phase transition in the 2 theta region of (44–46)° where the peak shifting were most actively observed, representing the MA behavior. The structural evolution was related to the broadening of peak intensity, which was considered to be the transition of Al(Cr) supersaturated solid solution. Brodova et al. reported [28] the formation behavior of the crystalline and amorphous Al–Cr alloy under rapid cooling. They demonstrated the formation of Al(Cr) supersaturated solid solution by substitution into Al and segregation in their grain boundaries due to discontinuous precipitation of fine Cr grains generated in the cooling and solidification process of Al–Cr alloy.

Prior to setting the sintering conditions, intermetallics with related invariant reactions (see Table 2) corresponding to the variation of temperature of the Al–Cr–Si ternary system was predicted using the Pandat software. In addition, Table 2 shows the reaction of Cr–Si binary and Al–Cr–Si ternary intermetallics through thermodynamic calculations reported in several studies [29–32]. In order to prevent the melting of Al_8Cr_5 phase, the sintering temperature was fixed to 1000 °C, which process was terminated in accordance with the melting behavior under the applied pressure of 60 MPa. Figure 4 presents that variation in shrinkage displacement–sintering temperature in $Al_{60}Cr_{30}Si_{10}$ compacts with their relative density. Due to the melting of Al-component at around 560 °C, the shrinkage displacement increased rapidly in the (5 and 15) h-milled powder, caused by the dominant distribution of single phases. On the other hand, the 25 h-milled powder being fully alloyed presents drastic shrinkage behavior from (580 to 1000) °C, which was considered to be due to consolidation close to the theoretical density by the formation and inter-diffusion of intermetallics [33].

Figure 5 shows the XRD patterns of the $Al_{60}Cr_{30}Si_{10}$ compacts for different milling time and sintering temperature.

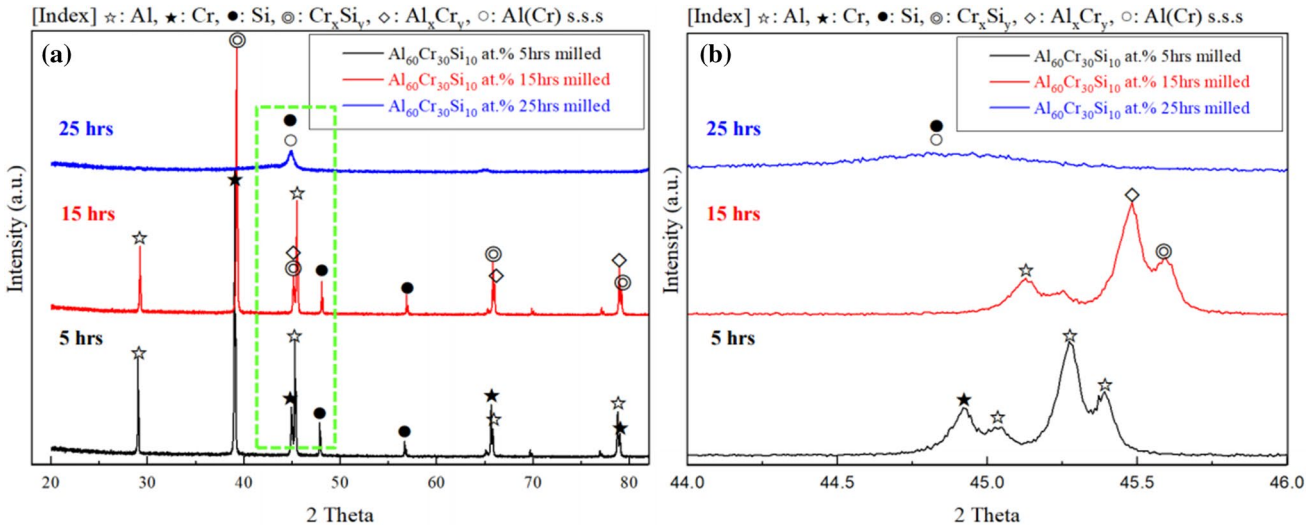

Fig. 3 XRD patterns of $Al_{60}Cr_{30}Si_{10}$ synthesized powders for different milling times: **a** 2 Theta (20–80)° range, and **b** peak shifting at the 2 Theta (44–46)° range by the mechanical alloying

Table 2 Invariant reaction with Intermetallics on Al–Cr–Si ternary alloy for each temperature derived from Pandat software and previous works

Temperature (°C)	Intermetallics [Ref.]
548	Al_9Cr_3Si (τ_2) [29]
577	$Al_{13}Cr_2$
625	$Al_{11}Cr_2$
718	Al_4Cr
801	αCr_5Si_3 [30]
862	Al_9Cr_4
912	Cr_3Si [31]
912	$AlCr_2$ [32]
914	Al_8Cr_5
1016	Al_8Cr_5 (melted)

Figure 5a shows that compacts by 5 h-milled powder detected only single phases (e.g. Al, Cr, and Si), because the Al-phase was melted to the liquid (L) state at around 560 °C, without being inter-diffused thermodynamically between adjacent phases at the corresponding temperature. Interestingly, intermetallics, such as $Al_3Cr_{15}Si_2$ and $Al_{0.98}Cr_{0.02}$, were observed in compacts prepared by the 15 h-milled powder, in conflict with the expectation that the distribution of single phases induced by Al-component melting would dominate. In fact, these metastable phases can be attributed to inter-diffusion for Al_9Cr_3Si (τ_2) phase referring to the invariant reaction around 548 °C (see Table 2) not being completed, and in which the ternary system bonds were dissociated by the melting of Al-component. However, Fig. 5b presents the structural evolutions in compacts by 25 h-milled powder in accordance with the variation of temperature.

Firstly, it was confirmed that the MAed powder having Al(Cr) supersaturated solid solution has a distribution of inter-diffused phases (e.g. Al_9Si, $Cr_{9.1}Si_{0.9}$) into the Al and Cr-rich corner embedding the Si single-phase when the temperature of 600 °C was applied. Hereby, the behavior of Si could be classified after high-pressure solidification into dissolution in Al-matrix, or precipitation as Si-rich phase in the interface Al–Si [34]. This was caused by the isomorphism of the Al–Si binary system. In addition, the formation of the Cr_3Si phase being metastable bonding was considered to be due to the decomposition of the Al-rich corner component in the Al_9Cr_3Si (τ_2) ternary intermetallics, which was unrelated to thermodynamic stability (see the invariant reaction at 912 °C in Table 2).

Secondly, at 1000 °C, several intermetallics were fully alloyed to consolidate into the Al-rich corner (e.g. Al_9Cr_3Si (τ_2), $Al_{13}Cr_2$, and Al_8Cr_5) and the Cr-rich corner (e.g. $AlCr_2$ and Cr_5Si_3) being the thermodynamically preferred phase, which were derived from two-sublattice behaviors by their relation of inherent solubility, respectively. Table 3 shows the details of their behaviors. In particular, the solubility of Si into Al_xCr_y structures rather tended to decrease with high temperatures. It was estimated that the intermetallics, which have been inter-diffused as thermodynamic steady state, were no longer able to dissolve the Si. In other words, unconsumed Si atoms were considered to terminate the reaction after finally forming Cr_5Si_3 phase via dissolution into the Cr within two-sublattices (see Table 3, i.e. the interface of Al_9Cr_3Si/Cr_5Si_3).

Finally, the Al_9Cr_3Si (τ_2) intermetallics due to melting of the Al_8Cr_5 component were observed at dominant peak intensity at 1100 °C. In particular, it is considered that the sintering immediately before the phase transition from $(Al,Si)_{11}Cr_4$ (τ_3) to $Al_{58}Cr_{31}Si_{11}$ (τ_4) in the temperature range [12] (1053–1083) °C were terminated, leading to

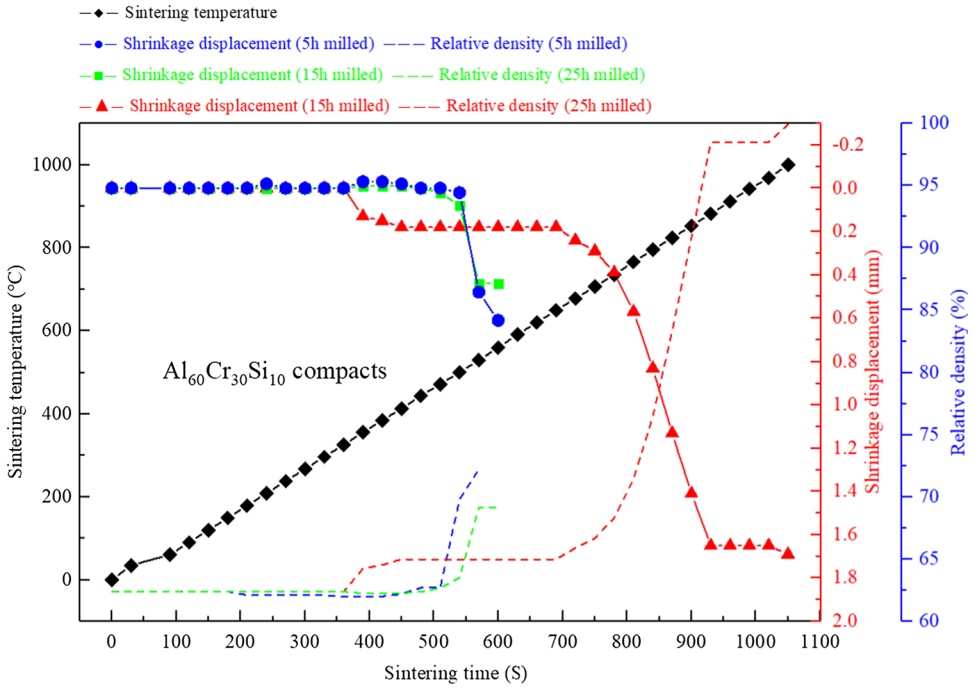

Fig. 4 Schematic of $Al_{60}Cr_{30}Si_{10}$ compacts with temperature and shrinkage displacement profile during the spark plasma sintering

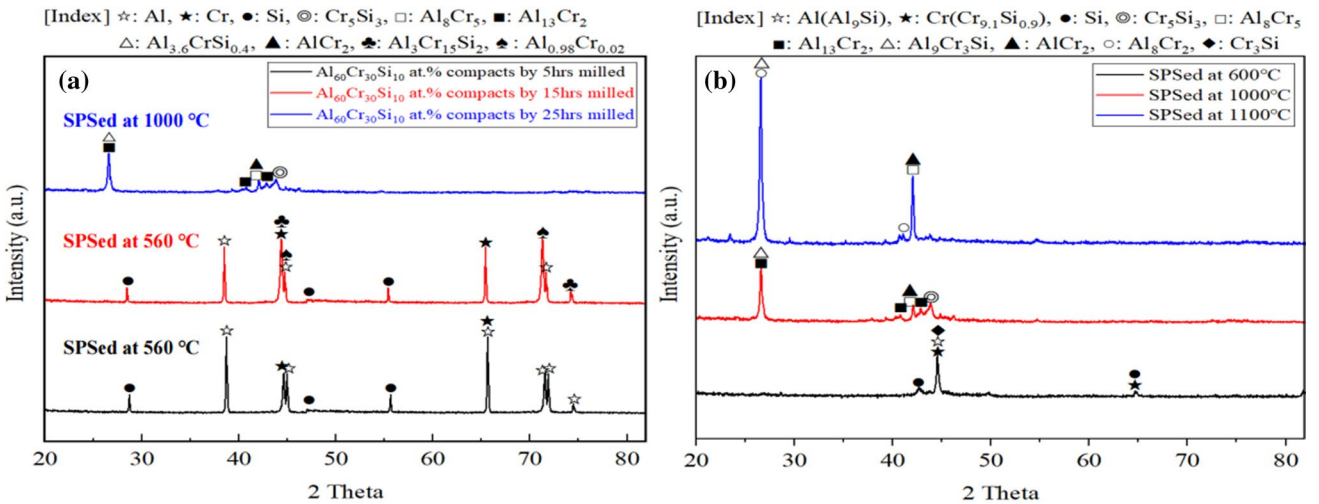

Fig. 5 XRD patterns of $Al_{60}Cr_{30}Si_{10}$ consolidated compacts: **a** for different milling times, and **b** phase transition of intermetallics in $Al_{60}Cr_{30}Si_{10}$ compacts (25 h milled) corresponding to each sintering temperature

Table 3 Details for two-sublattices and their solubility in $Al_{60}Cr_{30}Si_{10}$ sintered at 1000 °C

Intermetallics	Consists of two sublattices	Solubility information
$Al_9Cr_3Si(\tau_2)$ Cr_5Si_3	$(Al, Si)_{11}Cr_4(Al, Si)_{11}Cr_4$ (coexisting with Cr_5Si_3) [29]	Al, Si: first sublattice Cr: second one [29]
$Al_{13}Cr_2$	$(Al, Si)_{13}(Al, Cr)_2$	–
Al_8Cr_5	$(Al, Cr, Si)_8(Al, Cr, Si)_5$ [29]	~5.6 at% Si [29]
$AlCr_2$	$(Al, Cr, Si)(Al, Cr)_2$ [29]	(1.7–3.0) at% Si [32] (depends on temperature)

dominant behavior of the intermetallics with the Al–Cr–Si ternary system. In addition, the appearance of the Al_8Cr_2 metastable phase was believed to be formed by rapid solidification after the Al_8Cr_5 component was melted. Referring to the JCPDS card (40-1242) [35], this intermetallic forms a single phase with icosahedral structure, i.e. similarly to Mg_4Zn_7 phase growing on a quasicrystal [36].

Figure 6 shows the microstructural evolution in $Al_{60}Cr_{30}Si_{10}$ compacts, in which the EDS results in the specified regions were also presented. Figure 6a, which included regions from 1 to 3, confirmed that the single-phases were

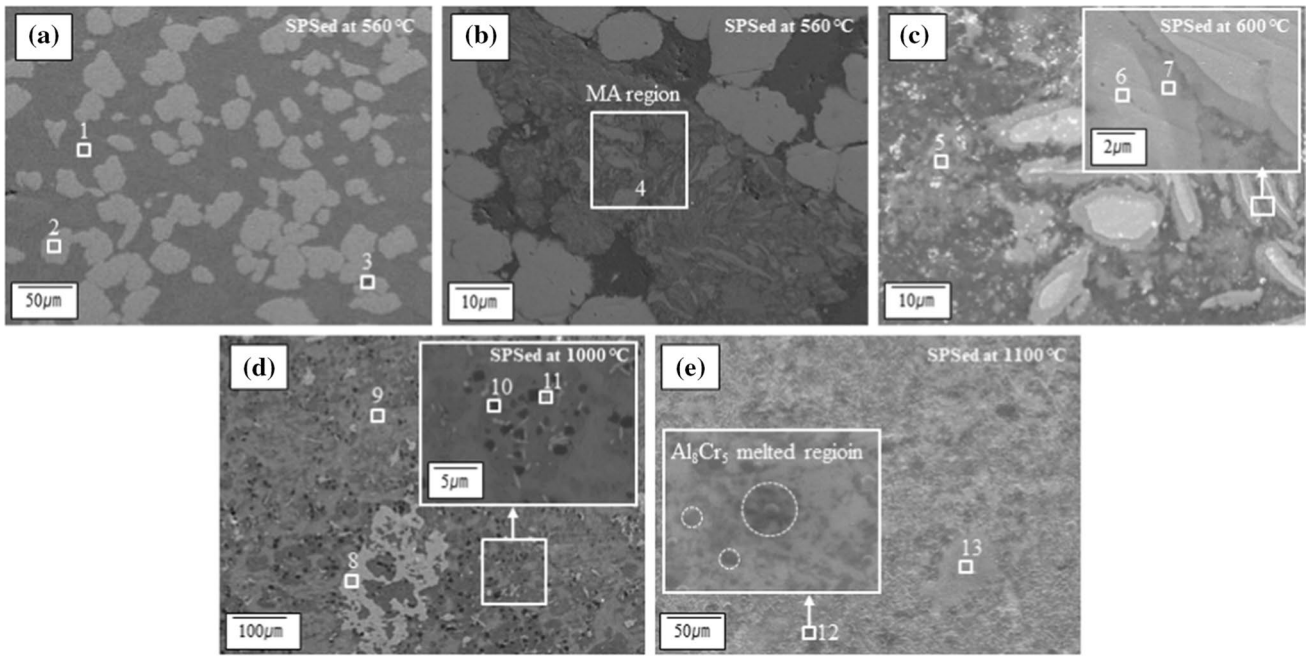

(f) Number	AlK (At.%)	CrK (At.%)	SiK (At.%)	Phase indexing
1	94.86	1.43	3.71	Al
2	1.95	0.68	97.37	Cr
3	1.10	1.71	97.19	Si
4	60.36	30.10	9.64	Al_xCr_y or $Al_xCr_ySi_z$
5	87.39	2.51	10.01	Al_9Si
6	5.94	84.01	10.05	$Cr_{9.1}Si_{0.1}$
7	9.34	65.38	25.29	Cr_3Si
8	3.32	58.67	38.01	Cr_5Si_3
9	69.01	21.86	9.13	Al_9Cr_3Si
10	76.68	42.28	1.03	Al_8Cr_5
11	80.24	2.82	16.93	$Al_{13}Cr_2$
12	29.55	68.73	1.73	$AlCr_2$
13	63.78	22.84	13.39	Al_9Cr_3Si

Fig. 6 FE-SEM micrographs of $Al_{60}Cr_{30}Si_{10}$ consolidated compacts processed by the various process conditions: **a** at 560 °C (5 h milled), **b** at 560 °C (15 h milled), **c** at 600 °C (25 h milled), **d** at 1000 °C (25 h milled), **e** at 1100 °C (25 h milled) and **f** EDS results and phase indexing with examining the regions

randomly distributed in compacts prepared by the 5 h-milled powder (see Fig. 6f, expressed as 1: Al, 2: Cr, and 3: Si). The MA region shown in Fig. 6b exhibits a typical lamellar structure, and was considered to be caused by the mechanical agglomeration of the 15 h-milled. As a result of the phase indexing, the non-stoichiometric composition distribution remained, which indicated only mechanical bonding before the inter-diffusion of the initial, i.e. Al_xCr_y or $Al_xCr_ySi_z$. Furthermore, Fig. 6c–e show the microstructures of the compacts fabricated by 25 h-milled powder in accordance with the correspondent of each temperature. At 600° C, between the Al rich-corner (see Fig. 6f, expressed as 5: Al_9Si) and

the Cr rich-corner interfaces showed the division into single-components, respectively. In particular, the Cr_3Si metastable phase (see Fig. 6c region (7) of dark-grey) formed by inter-diffusion with Si inner, the Cr phase (see Fig. 6c region (6) of grey) in the enlarged image within the interface was clearly investigated. At the 1000 °C, the distribution of intermetallics inner of fully densified compacts could be confirmed by the micro-morphology (see Fig. 6d). It was confirmed that the Cr_5Si_3 phase with chi-phase [37] morphology produced by polymorphic transition [38] was co-existent in the Al_9Cr_3Si (matrix), and in which the nano-sized Al_8Cr_5 and $Al_{13}Cr_2$ phases were embedded in the matrix phases (see the enlarged image for Fig. 6d). At 1100 °C, in the microstructures with the Al_9Cr_3Si intermetallics as a matrix, localized regions of the melted were observed to be distributed similar to the typical cast structure of powder metallurgy. In particular, the trace of melted Al_8Cr_5-component in the $AlCr_2$ phase rich-region was investigated in the enlarged regions.

Figure 7 shows the microstructural evolution of consolidated compacts with the concentration of intermetallics. In Fig. 7a, the heterogeneous distribution of intermetallics could be confirmed by the contrast shown in accordance with their difference of density in the BF image. Figure 7b shows the microstructure of the enlarged A-region, which was estimated to be $Al_{13}Cr_2$ intermetallics. Also, it was confirmed that their structural behaviors were preferentially oriented in the $(112)_m$ and $(023)_m$ planes by the FFT images converted from the diffraction patterns (the 'm' means with monoclinic structure). Likewise, Fig. 7c shows that the microstructural order was evident from the enlarged B-region, which was considered to be Al_8Cr_5 intermetallics having an irregular morphology. In particular Fig. 7d clearly shows evidence of the presence of two-sublattices for the co-existent Cr_5Si_3 in matrix phase (Al_9Cr_3Si). In addition, the behavior of inter-diffusion in the Cr_5Si_3 phase of peritectic type [39] was closely related to the two sublattice structure. In other words, since the formation of Al_9Cr_3Si phase was prioritized in the nearby Cr_5Si_3 phase, a certain amount of time was consumed in the diffusion, and the reaction proceeds in the form that the Al_9Cr_3Si phase surrounds the Cr_5Si_3 phase.

With reference to the FFT images, it can be confirmed that the diffraction patterns representing their crystal structures are overlapped, i.e. co-existent with the hexagonal/tetragonal structures based on the $[0001]_h$ and $[111]_t$ zone axes.

4 Conclusion

This study discussed the experimental proofs to clarify the microstructural and structural evolutions based on $Al_{60}Cr_{30}Si_{10}$ consolidated compacts prepared by mechanical alloying and rapid sintering with densification.

1. The $Al_{60}Cr_{30}Si_{10}$ powder was mechanically alloyed by their structural properties as the intermetallics, and peak shifting and broadening of the supersaturated solid solu-

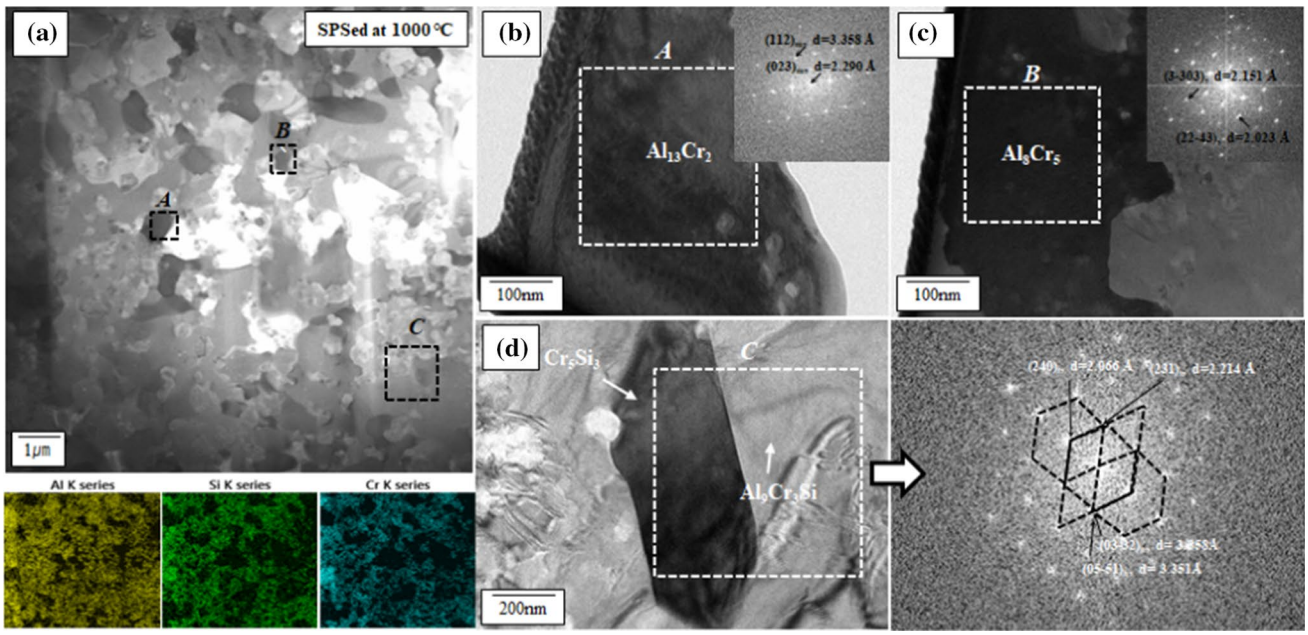

Fig. 7 Microstructural evolution of $Al_{60}Cr_{30}Si_{10}$ compacts with representative intermetallics by the FE-TEM and FFT images, i.e. 25 h milled powder and at SPS 1000 °C: **a** BF image and their mapping results, and **b**–**d** enlarged image of each region

tion from initial agglomeration to severe plastic deformation could be observed.
2. The $Al_{60}Cr_{30}Si_{10}$ compacts were rapidly consolidated by spark plasma sintering. Their microstructural evolution depends on the invariant reaction with the formation of thermodynamically stable phases, even so solubility and lattice structures.
3. The behavior of intermetallics was determined by the Al-rich corner (e.g. Al_9Cr_3Si, Al_8Cr_5, $AlCr_2$, $Al_{13}Cr_2$) or Cr-rich corner (Cr_3Si and Cr_5Si_3) components in accordance with the applied temperatures, in which the microstructural evidence was investigated using the SEM-mapping and FFT images of TEM.

Acknowledgements This study has been conducted with the support of the Korea Institute of Industrial Technology-Production Technology(KITECH)-Industry Leading Core Technology Development Project (1/4) as the "Development of a on-site facility attached cryogenic machining integrated system".

References

1. B.S. Kim, W.Y. Chung, M.H. Rhee, S.Y. Lee, Met. Mater. Int. **18**(6), 1023–1027 (2012)
2. J.H. Lee, H.K. Park, J.H. Jang, I.H. Oh, Met. Mater. Int. **25**, 268–276 (2019)
3. K.V. Smyrnova, A.D. Pogrebnjak, V.M. Beresnev, S.V. Litovchenko, S.O. Borba-Pogerebnjak, A.S. Manokhin, S.A. Klimenko, B. Zhollybekov, A.I. Kupchishin, Y.O. Kravchenko, O.V. Bondar, Met. Mater. Int. **25**(5), 1024–1035 (2018)
4. M.G. Faga, G. Gautier, F. Cartasegna, P.C. Priarone, L. Settineri, Appl. Surf. Sci. **365**, 218–226 (2016)
5. R. Forsen, M.P. Johansson, M. Oden, N. Ghafoor, Thin Solid Films **534**, 394–402 (2013)
6. M. Kawate, A.K. Hashimoto, T. Suzuki, Surf. Coat. Technol. **165**, 163 (2003)
7. O. Banakh, P.E. Schmid, R. Sanjines, F. Levy, Surf. Coat. Technol. **163–164**, 57–61 (2003)
8. W. Liu, Q. Chu, J. Zeng, R. He, H. Wu, Z. Wu, S. Wu, Ceram. Int. **43**(12), 9488–9492 (2017)
9. D. Philippon, V. Godinho, P.M. Nagy, M.P. Delplancke-Ogletree, A. Fernandez, Wear **270**, 541–549 (2011)
10. B. Hu, W.W. Zhang, Y. Peng, Y. Du, S. Liu, Y. Zhang, Thermchim. Acta **561**, 77–90 (2013)
11. S.P. Gupta, Mater. Charact. **52**, 355–370 (2004)
12. Y. Liang, C. Guo, C. Li, Z. Du, J. Phase Equilib. Diffus. **30**(5), 462–479 (2009)
13. J.S. Benjamin, Metall. Trans. **1**, 2943–2951 (1970)
14. M. Huang, K.Z. Li, Q.G. Fu, G.D. Sun, Carbon **45**, 1124–1126 (2007)
15. D.N. Zhang, Q.Q. Shangguan, F. Liu, M.Y. Zhang, Met. Mater. Int. **21**, 623–627 (2015)
16. E.K. Lee, C. Walde, B. Mishra, Met. Mater. Int. **24**, 815–820 (2018)
17. A.R. Stokes, A.J. Wilson, Math. Proc. Camb. Philos. Soc. **38**(3), 313–322 (1942)
18. B.C. Yu, K.C. Bae, J.K. Jung, Y.H. Kim, Y.H. Park, Met. Mater. Int. **24**(3), 576–585 (2018)
19. H.J. McQueen, Mater. Sci. Eng. A **387–389**, 203–208 (2004)
20. J.S. Benjamin, Sci. Am. **234**(5), 40–48 (1976)
21. P.S. Gilman, J.S. Benjamin, Annu. Rev. Mater. Sci. **13**, 279–300 (1983)
22. J.S. Benjamin, Met. Powder Rep. **45**, 122–127 (1990)
23. J.S. Benjamin, T.E. Volin, Metall. Trans. **5**, 1929–1934 (1974)
24. D.P. Riely, G.O. Jones, B.F. Figgins, Phys. Rev. **99**, 1737–1743 (1955)
25. G.T. Laissardiere, D.N. Manh, L. Magaud, J.P. Jullien, F.C. Lackmann, D. Mayou, Phys. Rev. B. **52**, 7920 (1995)
26. S.G. Jia, M.S. Zheng, P. Liu, F.Z. Ren, B.H. Tian, G.S. Zhou, H.F. Lou, Mater. Sci. Eng. A **419**(1–2), 8–11 (2006)
27. O. Brummer, W. Michel, Phys. Rev. **12**, 19 (1961)
28. I.G. Brodova, D.V. Bashlykov, I.G. Shirinkina, I.P. Lennikova, Mater. Sci. Forum **503–504**, 413–418 (2006)
29. H. Chen, F. Weitzer, J.C. Schuster, Y. Du, H. Xu, J. Alloys Compd. **436**, 313–318 (2007)
30. H. Chen, Y. Du, J.C. Schuster, CALPHAD **33**, 211–214 (2009)
31. L.F. Mondolfo, *Metallography of Aluminum Alloys*, vol. 74 (Wiley, New York, 1943)
32. A. Raman, K. Schubert, Z. Metallkd. **55**, 798–804 (1964)
33. K. Huang, Y. Park, A. Ewh, B.H. Sencer, J.R. Kennedy, K.R. Coffey, Y.H. Sohn, J. Nucl. Mater. **424**, 82 (2012)
34. E.V. Dedyaeva, T.K. Akopyan, A.G. Padalko, G.V. Talanova, G.I. Zubarev, A.D. Izotov, A.N. Suchkov, V.T. Fedotov, L.I. Shvorneva, Inorg. Mater **52**(10), 1077–1084 (2016)
35. D. Lawther, D. Dunlap, R. Srinvas, Can. J. Phys. **67**, 463 (1989)
36. A. Singh, J.M. Rosalie, Crystals **8**(5), 1–17 (2018)
37. J.S. Kasper, Acta. Metall. **2**, 456 (1956)
38. B.J. Kim, Y.S. Yun, W.T. Kim, D.H. Kim, Met. Mater. Int. **24**, 926–933 (2018)
39. C. Zhou, C. Guo, C. Li, Z. Du, *CALPHAD, Conference*, Singapore (2019)